ACS APPLIED MATERIALS & INTERFACES

Research Article

www.acsami.org

# Nitrogen-Doped Porous Carbon/$Co_3O_4$ Nanocomposites as Anode Materials for Lithium-Ion Batteries

Li Wang,[†] Yaolin Zheng,[†] Xiaohong Wang,[†] Shouhui Chen,[†] Fugang Xu,[†] Li Zuo,[†] Jiafeng Wu,[†] Lanlan Sun,[‡] Zhuang Li,[§] Haoqing Hou,[†] and Yonghai Song*[,†]

[†]Key Laboratory of Chemical Biology, Jiangxi Province, Key Laboratory of Functional Small Organic Molecule, Ministry of Education, College of Chemistry and Chemical Engineering, Jiangxi Normal University, 99 Ziyang Road, Nanchang 330022, China

[‡]State Key Laboratory of Luminescence and Applications, Changchun Institute of Optics, Fine Mechanics and Physics, Chinese Academy of Sciences, 3888 East Nan-Hu Road, Changchun 130033, China

[§]State Key Laboratory of Electroanalytical Chemistry, Changchun Institute of Applied Chemistry, Chinese Academy of Sciences, Changchun 130022, China

Supporting Information

**ABSTRACT:** A simple and industrially scalable approach to prepare porous carbon (PC) with high surface areas as well as abundant nitrogen element as anode supporting materials for lithium-ion batteries (LIBs) was developed. Herein, the N-doped PC was prepared by carbonizing crawfish shell, which is a kind of food waste with abundant marine chitin as well as a naturally porous structure. The porous structure can be kept to form the N-doped PC in the pyrolysis process. The N-doped PC-$Co_3O_4$ nanocomposites were synthesized by loading $Co_3O_4$ on the N-doped PC as anode materials for LIBs. The resulting N-doped PC-$Co_3O_4$ nanocomposites release an initial discharge of 1223 mA h $g^{-1}$ at a current density of 100 mA $g^{-1}$ and still maintain a high reversible capacity of 1060 mA h $g^{-1}$ after 100 cycles, which is higher than that of individual N-doped PC or $Co_3O_4$. Particularly, the N-doped PC-$Co_3O_4$ nanocomposites can be prepared in a large yield with a low cost because the N-doped PC is derived from abundant natural waste resources, which makes it a promising anode material for LIBs.

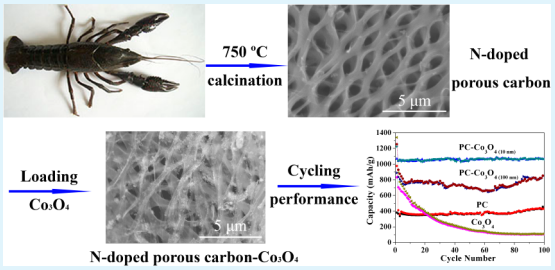


**KEYWORDS:** *N-doped porous carbon, $Co_3O_4$, nanocomposites, anode, lithium-ion batteries*

## 1. INTRODUCTION

Rechargeable lithium-ion batteries (LIBs) have attracted tremendous attentions because of the growing demand for low consumption, high energy density, long cycle life, and high efficiency.[1,2] The growing demand has stimulated intensive exploration of new electrode materials.[3]

Nanosized transition metal oxides such as $Co_3O_4$,[4−7] CoO,[8−10] $Fe_3O_4$,[11,12] $MnO_2$,[13] NiO,[14] and CuO[15] have been used as anode materials for LIBs because they possess higher specific capacities than commercial graphite (372 mA h $g^{-1}$).[11,16] Among them, $Co_3O_4$ shows excellent capacity retention and high rate performance because it can store more than eight lithium atoms per formula carbonaceous materials. However, the practical application of $Co_3O_4$ has been frustrated due to the large volume expansion-contraction and severe particle aggregation, which always leads to electrode pulverization, capacity loss and poor cycling stability.[17] To overcome these limitations, an effective way to enhance the electrochemical performance is to combine $Co_3O_4$ with carbon materials.

Carbon materials has attracted growing interests because of its essential properties such as high electronic conductivity, good corrosion resistance and a series of surface properties,[2,18] which are required for the commercialization of LIBs. Various carbon materials such as graphene and carbon nanotubes (CNTs) have been used in LIBs because of their high specific surface area and the perfect electrical transmission performance.[19−21] However, the overlapping of graphene sheets is the critical challenges during electrode preparation and electrochemical test. The high production costs and purification difficulty also limit CNTs widespread applications.[22,23] Therefore, low-cost carbon with high surface area, good electrical conductivity, and porous structures would probably be the most suitable supporting materials for LIBs. Recently, biomaterials-derived porous carbon (PC) has attracted tremendous attentions due to its low production cost, large specific surface area, accessible surface chemistry and short diffusion pathway for ions.[24−34] Lots of biomaterials with porous structure have been directly carbonized to form N-doped PC materials.[28,35−37] The doping of N atom in PC introduces the donor states near the Fermi level to generate n-type conductive materials.[38] The well-bonded N atom provides more active sites to increase the

Received: January 2, 2014
Accepted: May 6, 2014
Published: May 6, 2014

  

interaction between the carbon and adsorbents, thus it is expected to improve electrochemical performance.[39] The crawfish shell is the food waste, which as precursor is economic and environmentally friendly. Because of the large amount of nitrogen elements and excellent porous structure, the N-doped PC derived from crawfish shell could be a promising material to replace graphene and CNTs for LIBs.[40−42]

In this work, N-doped PC-$Co_3O_4$ nanocomposites were successfully synthesized via a facile hydrothermal method using natural porous crawfish shells as the carbon source. The N-doped PC has a large number of nitrogen functional groups, which provides more binding sites to enhance the deposition of $Co_3O_4$. The composition structure of N-doped PC-$Co_3O_4$ nanocomposites could effectively alleviate the aggregation of $Co_3O_4$ in the $Li^+$ insertion/extraction to avoid the rapid capacity fading.[43−45] The as-prepared nanocomposites as a low-cost anode material for LIBs exhibited high lithiation capacity, good rate capability, and excellent cycle performance.

## 2. EXPERIMENTAL SECTION

**2.1. Reagents and Materials.** The crawfish used in this study is "small tiger crawfish" and obtained from local marketplace (Nanchang, China). $Co(CH_3COO)_2{\cdot}4H_2O$ was obtained from Sigma-Aldrich. Acetic acid and $NH_3{\cdot}H_2O$ (25−28 wt %) were purchased from Tianjin Yongda Chemical Reagent Factory (Tianjin, China). Other reagents were purchased from Beijing Chemical Reagent Factory (Beijing, China). Polyvinylidene fluoride (PVDF, Lefu Shanghai Chemicals), carbon black (Kaisai Shanghai Chemicals), copper foil (10 $\mu$m thickness, Jiayuan Guangzhou Company) and metallic Li foil (0.6 mm thickness, 99.9%, Zhongneng Tianjin Company) was used without further treatment. Other chemicals used in this study are analytical grade. All solutions were prepared with ultrapure water, purified by a Millipore-Q System (18.2 MΩ cm).

**2.2. Preparation of N-Doped PC.** The crawfish shell-derived N-doped PC was prepared as Scheme 1. First, the crawfish were cooked

**Scheme 1. Fabrication Process of the Crawfish Shell-Derived PC-$Co_3O_4$ Nanocomposites**

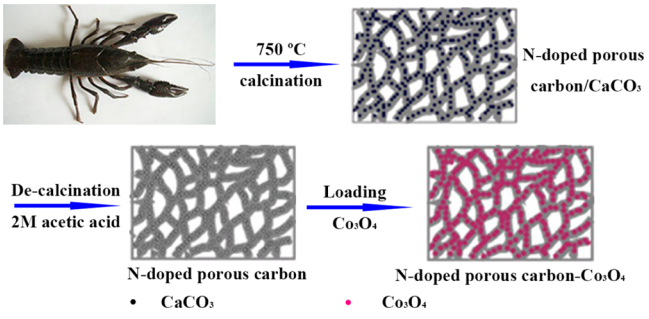


in boiling water for 1 h to separate the crawfish meat and crawfish shell completely. Then, the crawfish shells were peeled off from the crawfish, washed by ultrapure water, and dried in an oven at 80 °C. After that, the crawfish shells were carbonized in a tubular quartz reactor under $N_2$ atmosphere with a heating rate of 3 °C $min^{-1}$ and annealing at 750 °C for 4 h. And then, the black solid was added into 2.0 M acetic acid solution and stirred for 36 h to eliminate $CaCO_3$. Finally, the sample was extensively washed with ultrapure water, and dried at 80 °C overnight under vacuum to obtain the N-doped PC.

**2.3. Synthesis of N-Doped PC-$Co_3O_4$ Nanocomposites.** In a typical procedure,[46] 70 mg of N-doped PC was added into 96 mL of EtOH, and then ultrasound dispersed for 30 min. Next, 4.4 mL of water and 0.36 g of $Co(CH_3COO)_2{\cdot}4H_2O$ was added into above solution under stirring and then 2 mL of 28% ammonia was added. After that, the mixture was stirred for 20 h at 80 °C. Lastly, the mixed product (about 60−70 mL) was transferred into a Teflon-lined stainless steel autoclave with a volume of 100 mL, and a thermal treatment was performed in an oven at 150 °C for 3.5 h. The product was centrifuged and washed with ethanol and water to obtain the N-doped PC-$Co_3O_{4\ (10\ nm)}$ nanocomposites. The effects of time (see Figure S1 in the Supporting Information) and temperature (see Figure S2 in the Supporting Information) in the thermal treatment on the N-doped PC-$Co_3O_4$ nanocomposites have been explored. According to a similar procedure (see the Supporting Information), the N-doped PC-$Co_3O_4$ nanocomposites with 100 nm $Co_3O_4$ nanoparticles (N-doped PC-$Co_3O_{4\ (100\ nm)}$) are also prepared. The characteristics of N-doped PC-$Co_3O_{4\ (100\ nm)}$ are shown in Figures S3 and S4 (see the Supporting Information).

**2.4. Characterizations.** Scanning electron microscopy (SEM) analysis was taken using a XL30 ESEM-FEG SEM at an accelerating voltage of 20 kV equipped with a Phoenix energy dispersive X-ray analyzer (EDXA). X-ray powder diffraction (XRD) data were collected on a D/Max 2500 V/PC X-ray powder diffractometer using Cu K$\alpha$ radiation ($\lambda$ = 1.54056 Å, 40 kV, 200 mA). X-ray photoelectron spectroscopy (XPS) was performed using an ESCA-LAB-MKII spectrometer (VG Co., United Kingdom) with $Al_{K\alpha}$ X-ray radiation as the source for excitation. Nitrogen content was obtained from Elemental Analyzer-EA3000 (EuroVector, Italy). Thermogravimetric analysis (TGA) was conducted on SDT 2960 with a heating rate of 10 °C $min^{-1}$. The surface areas (BET) of the samples were determined after degassing the samples at 300 °C and analyzing the $N_2$ adsorption isotherm at liquid nitrogen temperature (Tristar 3000). Transmission electron microscopy (TEM), high resolution TEM (HRTEM), and the selected area electron diffraction (SAED) were carried out on a JEM-2010 (HR) microscope.

**2.5. Electrochemical Measurements.** The working electrodes were made by a slurry coating procedure. The slurry was consisted of 80 wt % N-doped PC-$Co_3O_4$ nanocomposites, 10 wt % black carbon and 10 wt % PVDF dissolved in *N*-methylpyrrolidinone. This slurry was spread uniformly on copper foil, which acted as a current collector. The electrodes were dried in an oven at 60 °C for overnight, and then dried in a vacuum oven at 120 °C for 5 h. The active materials loading on copper foil is about 0.8 mg/$cm^2$. The celgard 2300 microporous polypropylene film was used as separator. The cells were assembled in an argon-filled glovebox using Li foil as counter electrodes. The electrolyte was made of 1.0 M $LiPF_6$ dissolved in a 1:1 (v/v) mixture of ethylene carbonate and dimethyl carbonate. Electrochemical impedance spectroscopy (EIS) was carried out with a CHI 760D electrochemical workstation (CH Instruments, Shanghai, China) using a conventional three-electrode system with Li metal as the counter and reference electrode, active materials as the working electrode. Other electrochemical experiments were carried out in two-electrode coin cells. The electrochemical discharge/charge tests of the samples were performed on a Neware BTS test system (Shenzhen, China) at voltage limits of 3.0−0.01 V versus Li/$Li^+$.

## 3. RESULTS AND DISCUSSION

The morphologies of as-synthesized N-doped PC derived from crawfish shell are first characterized by SEM. As shown in the overview image of a piece of N-doped PC (Figure S5 in the Supporting Information), a large number of relatively uniform sheet-by-sheet paperlike PCs are observed. Panels a and b in Figure 1 show the fine structures of N-doped PC. The obtained N-doped PC materials have two unique ordered macropores with an average diameter of about 1.0−2.0 $\mu$m (Figure 1a, network hole, the crawfish shell adjacent to crawfish meat tissue) and 0.5−1.0 $\mu$m (Figure 1b, round hole, the crawfish shell far from crawfish meat tissue), respectively. It is difficult to separate these two porous structures. Therefore, both of the porous structures are used as the supporting material for loading $Co_3O_4$ in the subsequent experiments. The macropores should result from the naturally porous structure of crawfish shell which was kept to form the N-doped PC in the pyrolysis process.

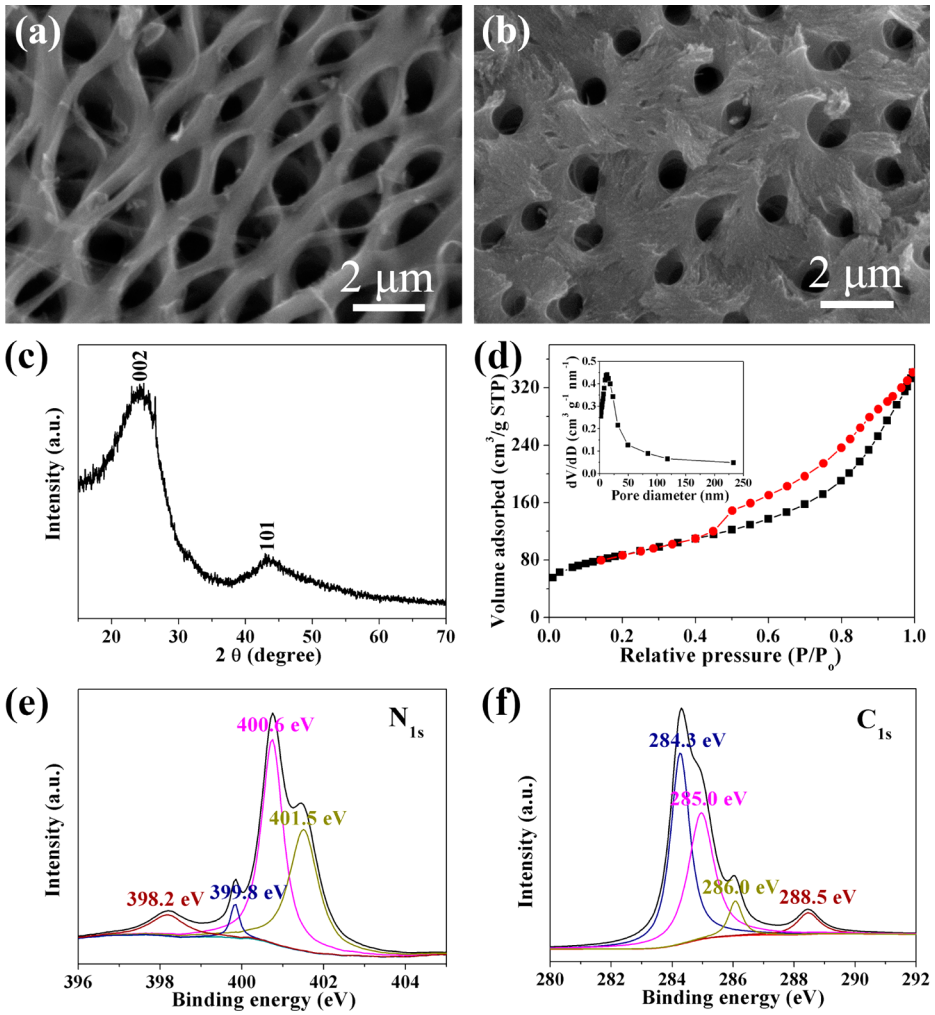


**Figure 1.** (a,b) SEM images of N-doped PC derived from crawfish shell: (a) network hole and (b) round hole. (c) XRD pattern, (d) $N_2$ adsorption/desorption isotherm, (e) $N_{1s}$ XPS spectra, and (f) $C_{1s}$ XPS spectra of the N-doped PC. Inset in d is the pore-size distribution calculated from the adsorption branch by the BJH model of the N-doped PC.

The structures of the as-prepared N-doped PC were also studied by X-ray diffraction (XRD) (Figure 1c). The diffraction peaks located at 24.7 and 43.2° correspond to the (002) and (101) diffraction planes of PC (JCPDS No. 41−1487), respectively.[7,21,28] The strongest diffraction in the XRD pattern at 24.7° is attributed to the formation of graphite layers in the N-doped PC.[47] $N_2$ adsorption/desorption experiments were performed to examine the pore size distribution and surface areas of the N-doped PC materials (Figure 1d). The N-doped PC exhibits a BET surface area of 304.4 $m^2\ g^{-1}$ and a total pore volume of 0.487 $cm^3\ g^{-1}$. As presented in the inset of Figure 1d, the average pore size of the N-doped PC materials was 6.4 nm, indicating the N-doped PC contains macropores and mesopores in the nanosheets. The mesopores may result from the removal of nanosized $CaCO_3$ and the decomposition of some biological organization. Such porous structure will not only facilitates fast lithium ion transport, but also provides an easy access way for electrolyte in LIBs.

After heat treatment, the elemental distribution of C, O, and N in the N-doped PC was examined by XPS as shown in Figure S6 (SI). The N atom in N-doped PC can introduce defect structure as the active sites for the deposition of $Co_3O_4$.[42,48,49] As shown in Figure 1e, there are three kinds of N in the N-doped PC: pyridine-like N (398.2 eV, a N atom bonding with two carbon atoms), pyrrolic N (399.8 and 400.6 eV) and graphite-like N (401.5 eV, a N atom replacing a graphitic C atom).[32,42,48,49] The pyridine-like N can directly bond with metal atoms and graphite-like N can mediate their neighboring C atoms to bond with metal atoms, which is beneficial to deposition of $Co_3O_4$.[42,48,49] It is necessary to explain, there are no discussion to the N oxides because their compositions are low. The N-doping can also be confirmed by the elemental analysis and the amount of N is about 4.1% (see Table S1 in the Supporting Information).

The fine-scanned $C_{1s}$ spectrum is displayed in Figure 1f. Among the four photon energies, an asymmetric $C_{1s}$ spectrum centered at 284.3 eV is C−C group of graphite.[48,49] The peak at 285.0 eV reflects bonding structure of the C−N bonds, corresponding to the N-$sp^2$ C bonds, which may originate from substitution of the N atoms and defects or the edge of the N-doped PC.[48,49] Due to the higher electronegativity of N atoms, the weakest peak at 288.5 eV is ascribed to the other binding configurations such as O−C═O that can be formed at the edge of N-doped PC.[48,49] The peak at 286.0 eV is attributed to C−O groups in the N-doped PC.[48,49] The result suggests that the surface of the N-doped PC generates large amounts of N and O groups after calcination treatment.


dx.doi.org/10.1021/am406053s | ACS Appl. Mater. Interfaces 2014, 6, 7117−7125

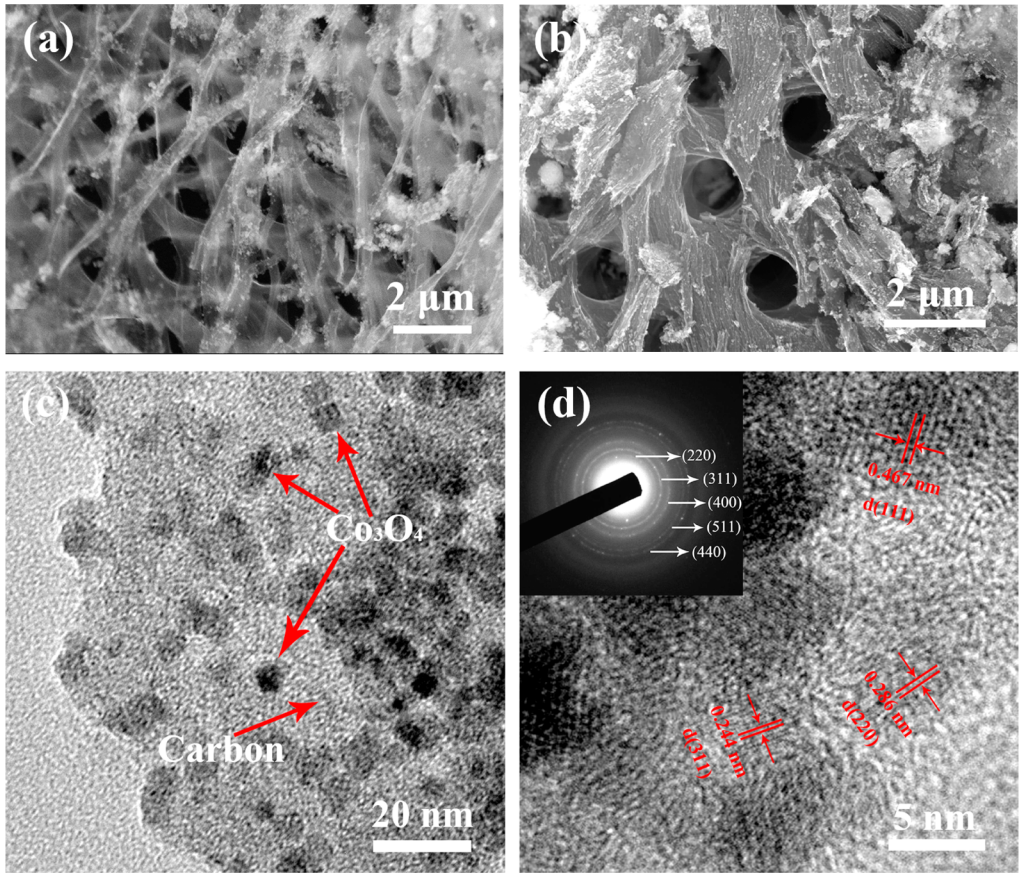


**Figure 2.** (a, b) SEM, (c) TEM, (d) HRTEM, and (inset in d) SAED images of the N-doped PC-$Co_3O_4$ $_{(10\ nm)}$ nanocomposites.

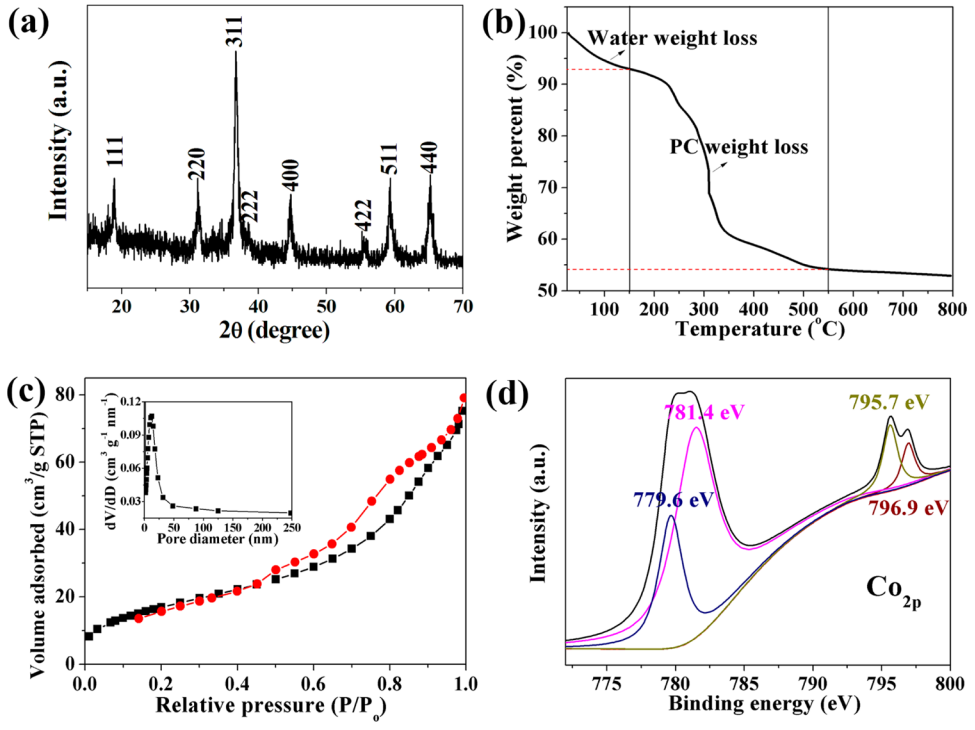


**Figure 3.** (a) XRD pattern, (b) TGA curve, (c) $N_2$ adsorption/desorption isotherm, and (d) $Co_{2p}$ XPS of the N-doped PC-$Co_3O_4$ $_{(10\ nm)}$ nanocomposites. Inset in c is the pore-size distribution calculated from the adsorption branch by the BJH model of N-doped PC-$Co_3O_4$ $_{(10\ nm)}$ nanocomposites.


dx.doi.org/10.1021/am406053s | ACS Appl. Mater. Interfaces 2014, 6, 7117−7125

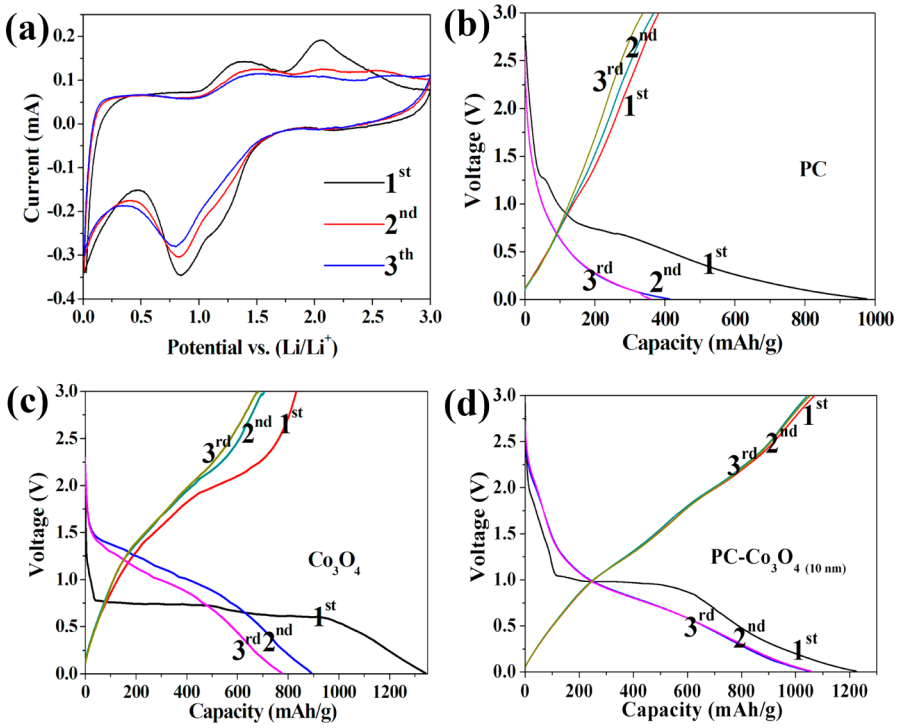


**Figure 4.** (a) CV curves of the N-doped PC-$Co_3O_4$ (10 nm) nanocomposite electrode at 0.2 mV/s. (b–d) Galvanostatic charge/discharge profiles of (b) the N-doped PC, (c) pure $Co_3O_4$, and (d) the N-doped PC-$Co_3O_4$ (10 nm) for the 1st, 2nd, and 3rd cycling.

Images a and b in Figure 2 show the SEM images of N-doped PC-$Co_3O_4$ (10 nm) nanocomposites. The images show the $Co_3O_4$ nanoparticles (white spot) are uniformly anchored on the N-doped PC nanosheets, and both kinds of porous structures are well preserved. TEM was also employed to identify the size of $Co_3O_4$ as shown in Figure 2c. It clearly demonstrates that the $Co_3O_4$ nanoparticles with size of 5–10 nm were evenly distributed on the surface of N-doped PC. HRTEM was also employed to analyze the lattice stripes of the N-doped PC-$Co_3O_4$ (10 nm) nanocomposites. As shown in Figure 2d, the lattice spacing of 0.467, 0.286, and 0.244 nm correspond to the (111), (220), (311) crystal planes of $Co_3O_4$, respectively. Inset of Figure 2d shows a typical selected-area electron diffraction (SAED) pattern of the $Co_3O_4$ nanocomposites. The diffraction rings correspond to (220), (311), (400), (511), and (440) planes of polycrystalline $Co_3O_4$, indicating the formation of $Co_3O_4$ crystal. The relatively even distribution and size of $Co_3O_4$ nanoparticles may be ascribed to a large number of N and O groups of N-doped PC, which not only provide many anchor sites for the uniform deposition of $Co_3O_4$ nanoparticles but also enhance the interaction between $Co_3O_4$ nanoparticles and N-doped PC by coordination interaction as discussed above.

The crystal structure of the as-prepared N-doped PC-$Co_3O_4$ (10 nm) nanocomposites was characterized by XRD as shown in Figure 3a. The characteristic diffraction peaks at 18.9, 31.22, 36.77, 38.5, 44.71, 55.62, 59.25, and 65.13° were observed, corresponding to the (111), (220), (311), (222), (400), (422), (511), and (440) crystalline planes of $Co_3O_4$, respectively (JCPDS No. 42–1467),[4,8,50,51] in good agreement with the HRTEM and SAED pattern in Figure 2d.

Figure 3b shows the TGA curve of N-doped PC-$Co_3O_4$ (10 nm). The weight loss before 150 °C can be mainly attributed to water loss. The second weight loss step in the range of 150–550 °C is mostly due to the burning of N-doped PC and the remnants after 550 °C should be attributed to $Co_3O_4$. Based on the TGA, the weight percentage of $Co_3O_4$ and N-doped PC are about 57.6 and 42.4 wt %, respectively.[51] $N_2$ adsorption/desorption isotherms at 77 K was used to characterize the porous structure of N-doped PC-$Co_3O_4$ (10 nm) nanocomposites (Figure 3c). The isotherm is characteristic of a type IV with type H3 hysteresis loop, which confirms the existence of the mesoporous structure. After loading of $Co_3O_4$ nanoparticles, the BET surface area of N-doped PC-$Co_3O_4$ (10 nm) nanocomposites is calculated to be 65.1 $m^2\ g^{-1}$ and total pore volume is 0.107 $cm^3\ g^{-1}$. The pore size distribution is also shown in the inset of Figure 3c, indicating an average pore size at about 6.87 nm. The differences in BET surface area between the N-doped PC (304.4 $m^2\ g^{-1}$) and N-doped PC-$Co_3O_4$ (10 nm) (65.1 $m^2\ g^{-1}$) nanocomposites might be due to the much larger density of $Co_3O_4$ with large molecular weight being anchored on the N-doped PC.

The N-doped PC-$Co_3O_4$ (10 nm) nanocomposites were also characterized by XPS spectrum as shown in Figure S7a (see the Supporting Information). The sharp peaks at 285.9, 532.2, and 780.8 eV correspond to the characteristic peaks of $C_{1s}$, $O_{1s}$, and $Co_{2p}$, respectively, indicating the existence of C, O, and Co elements in the sample. The doped N and O atoms can coordinate with $Co^{2+}$, which provide favorable nucleation and more anchoring sites for the uniform deposition of $Co_3O_4$ nanoparticles.[52] The disappearance of $N_{1s}$ signal in the N-doped PC-$Co_3O_4$ (10 nm) nanocomposites further confirmed that the $Co_3O_4$ nanoparticles are bond with the N-related defective sites.[48] Figure S7b (see the Supporting Information) shows the XPS spectra of $C_{1s}$ of N-doped PC-$Co_3O_4$ nanocomposites. The $C_{1s}$ XPS spectra of PC-$Co_3O_4$ nanocomposites are similar to the N-doped PC. The $Co_{2p}$ photoelectrons have also been investigated to probe surface metal species (Figure 3d). The $Co_{2p1/2}$ and $Co_{2p3/2}$ spectra can be deconvoluted into four peaks at 795.7 and 796.9 eV for


dx.doi.org/10.1021/am406053s | ACS Appl. Mater. Interfaces 2014, 6, 7117–7125

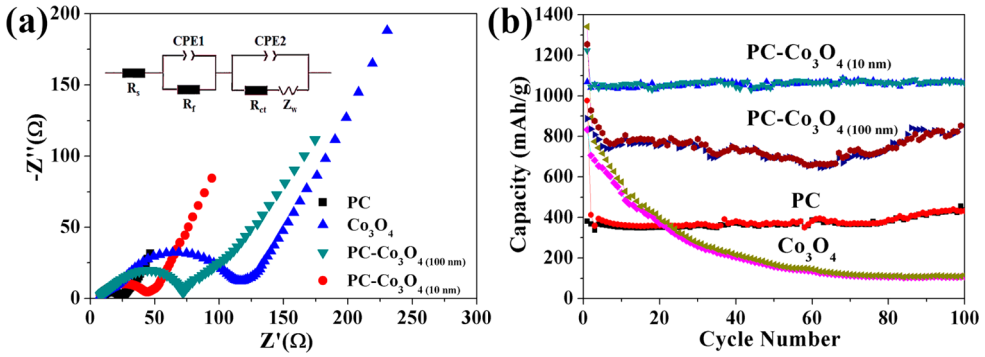


**Figure 5.** (a) Nyquist plots of the N-doped PC, $Co_3O_4$, N-doped PC-$Co_3O_{4\ (100\ nm)}$, and N-doped PC-$Co_3O_{4\ (10\ nm)}$ nanocomposites electrode. Inset: the equivalent circuit used for fitting impedance spectra. (b) Cycling performance of the N-doped PC, $Co_3O_4$, N-doped PC-$Co_3O_{4\ (100\ nm)}$, and N-doped PC-$Co_3O_{4\ (10\ nm)}$ nanocomposites at a current density of 100 mA $g^{-1}$.

$Co_{2p1/2}$, 779.6 and 781.4 eV for $Co_{2p3/2}$, respectively,[51,52] showing a characteristic of $Co_3O_4$ phase.

Cyclic voltammograms (CVs) tests were further carried out to evaluate the electrochemical performance of the N-doped PC-$Co_3O_{4\ (10\ nm)}$ nanocomposites at 0.2 mV $s^{-1}$ over the voltage range from 0.01 to 3.00 V (Figure 4a). The peaks around 0.8 and 1.2 V in the first cycle are attributed to the reduction of $Co_3O_4$ to Co as well as the formation of solid electrolyte interface (SEI, $Li_2O$) on the surface of N-doped PC-$Co_3O_{4\ (10\ nm)}$.[4,8,50,51] The electrochemical reaction mechanism of $Li^+$ with $Co_3O_4$ can be described as follows[4,8,50,51,53]

$$Co_3O_4 + 8Li^+ + 8e^- \leftrightarrow 4Li_2O + 3Co \quad (1)$$

$$8Li \leftrightarrow 8Li^+ + 8e^- \quad (2)$$

Typical charge−discharge curves of the N-doped PC, $Co_3O_4$ and N-doped PC-$Co_3O_{4\ (10\ nm)}$ nanocomposites electrode at the current density of 100 mA $g^{-1}$ for the first, second, and third cycles are shown in Figure 4b−d, respectively. The N-doped PC exhibits superior electrochemical properties with respect to $Li^+$ insertion and extraction without any voltage plateaus (Figure 4b), whereas both pure $Co_3O_4$ (Figure 4c) and N-doped PC-$Co_3O_{4\ (10\ nm)}$ (Figure 4d) nanocomposites exhibit long voltage plateaus in the first discharge step, which might result from the formation of $Li_2O$ and Co. It indicates the typical characteristics of the voltage profile for $Co_3O_4$ electrodes. It is noticeable that reversible decomposition and formation of the $Li_2O$ can be electrochemically driven by the nanosized transition metal particles during charged process.[50]

Nyquist plots of the N-doped PC, $Co_3O_4$, N-doped PC-$Co_3O_{4\ (100\ nm)}$, and N-doped PC-$Co_3O_{4\ (10\ nm)}$ electrode were performed in the frequency range of 100 kHz to 0.01 Hz at room temperature (Figure 5a). The Nyquist plot for the electrodes consists of a semicircle at high frequency and an inclined line at low frequency. The high-frequency semicircle is attributed to the SEI film, contact resistance, and the charge-transfer impedance on electrode/electrolyte interface. And the inclined line corresponds to the lithium-diffusion process within electrodes.[17,54] The equivalent circuit used for fitting impedance spectra is shown in inset of Figure 5a, where $R_s$ refers to the electrolyte resistance, $R_f$ and $CPE_1$ are the resistance and capacitor of the surface film formed on the electrodes, $R_{ct}$ and $CPE_2$ are the double-layer charge-transfer resistance and capacitance, and $Z_w$ is the Warburg impedance related to the diffusion of lithium ions into the bulk of the electrodes. The value of the $R_s$, $R_f$, and $R_{ct}$ calculated through fitting the impedance spectra are shown in Table S2 in the Supporting Information. Obviously, both the $R_f$ and $R_{ct}$ for the N-doped PC-$Co_3O_{4\ (10\ nm)}$ are lower than those for pure $Co_3O_4$, implying the N-doped PC-$Co_3O_{4\ (10\ nm)}$ has a thinner SEI film and a faster $Li^+$ diffusion rate.[7] The thickness of SEI film over active electrode might affect the performance of a given electrode. The large slope of inclined line in EIS indicates the fast lithium-diffusion process of the N-doped PC-$Co_3O_{4\ (10\ nm)}$ nanocomposites.[17] The larger impedance of N-doped PC-$Co_3O_{4\ (100\ nm)}$ electrode as compared with N-doped PC-$Co_3O_{4\ (10\ nm)}$ is possibly due to the larger size of $Co_3O_4$, which reduces the conductivity of the electrode.

A comparison of the charge/discharge cycling performance of the N-doped PC, $Co_3O_4$, N-doped PC-$Co_3O_{4\ (100\ nm)}$, and N-doped PC-$Co_3O_{4\ (10\ nm)}$ nanocomposites at a current density of 100 mA $g^{-1}$ is shown in Figure 5b. It is found that the capacity of N-doped PC is about 400 mA h $g^{-1}$ after 100 cycles, which is much higher than that of commercial graphite (372 mA h $g^{-1}$).[11,16] Thus, it is expected to replace graphite in industrial production. The N-doped PC-$Co_3O_{4\ (10\ nm)}$ nanocomposite exhibits much better electrochemical lithium storage performance than N-doped PC, $Co_3O_4$ and N-doped PC-$Co_3O_{4\ (100\ nm)}$. The N-doped PC-$Co_3O_{4\ (10\ nm)}$ nanocomposite maintains the reversible capacity well and exhibits a high reversible capacity of 1060 mA h $g^{-1}$ after 100 cycles, whereas it can be seen that the reversible capacity of $Co_3O_4$ decreases from 833 to only 109 mA h $g^{-1}$. In addition, the initial discharge and charge capacities of the N-doped PC-$Co_3O_{4\ (10\ nm)}$ nanocomposites are 1223 and 1060 mA h $g^{-1}$, respectively. The initial Coulombic efficiency is 86.7%. It is higher than that of N-doped PC-$Co_3O_{4\ (100\ nm)}$, whose initial discharge and charge capacities are 1256 and 886 mA h $g^{-1}$ and Coulombic efficiency is 70.5%, suggesting the size of $Co_3O_4$ nanoparticles also plays an important role in electrochemical performance. The high capacity of the initial discharge process in N-doped PC-$Co_3O_{4\ (10\ nm)}$ nanocomposites might be caused by the formation of SEI film. The high capacity and good cycling stability of the N-doped PC-$Co_3O_{4\ (10\ nm)}$ nanocomposite can be attributed to the synergetic effects of the two components. The good conductivity and porous N-doped PC not only serves as the physical support to load a large number of $Co_3O_4$ but also provides the channels for charge and mass transport.[52] Furthermore, the porous structure of N-doped PC-$Co_3O_{4\ (10\ nm)}$ can effectively alleviate the aggregation of $Co_3O_4$ in the $Li^+$ insertion/extraction to avoid the rapid capacity fading.[55]

Table 1. Comparison of the Performance of Carbon/$Co_3O_4$ Nanocomposites As Anode Materials for Lithium Ion Batteries

| active material | current density mA $g^{-1}$ | reversible capacity mA h $g^{-1}$ | cycle life | initial Coulombic efficiency (%) | ref |
|---|---|---|---|---|---|
| CNT/$Co_3O_4$ | 200 | 823 after 60 cycles | 96.8% retention during 60 cycles | 66.7 | 51 |
| carbon/Co metal | 50 | 600 after 40 cycles | 95.2% retention during 40 cycles | 55.0 | 56 |
| carbon/$Co_3O_4$ | 100 | 534 after 20 cycles | 69.8% retention during 20 cycles | 66.8 | 57 |
| carbon/$Co_3O_4$ | 50 | 779 after 50 cycles | 86.1% retention during 50 cycles | 50.4 | 58 |
| graphene/CoO | 100 | 1401 after 60 cycles | | 60.3 | 9 |
| graphene/$Co_3O_4$ | 50 | 1003 after 50 cycles | 90.6% retention during 50 cycles | 86.2 | 59 |
| graphene/$Co_3O_4$ | 50 | 935 after 30 cycles | | 68.6 | 4 |
| graphene/$Co_3O_4$ | 89 | 1065 after 30 cycles | 86.3% retention during 30 cycles | 53.7 | 60 |
| graphene/$Co_3O_4$ | 100 | 840 after 40 cycles | 83.5% retention during 40 cycles | 71.6 | 61 |
| N-doped PC-$Co_3O_{4\ (100\ nm)}$ | 100 | 851 ± 68 after 100 cycles | (96.0 ± 1.3)% retention during 100 cycles | (70.5 ± 4.5)% | this work |
| N-doped PC-$Co_3O_{4\ (10\ nm)}$ | 100 | 1060 ± 74 after 100 cycles | (97.7 ± 1.5)% retention during 100 cycles | (86.7 ± 4.7)% | this work |

Rate performance of the nanocomposites may be important in terms of commercial applications. As shown in Figure S8 (see the Supporting Information), the capacities of N-doped PC-$Co_3O_{4\ (10\ nm)}$ can recover back to 704 mA h $g^{-1}$ after cycles test, demonstrating the excellent recyclability of nanocomposites. At a high current rate, the N-doped PC-$Co_3O_{4\ (10\ nm)}$ nanocomposites exhibit highly reversible capacity and excellent cycling stability in lithium-ion storage and retrieval. Therefore, the N-doped PC-$Co_3O_{4\ (10\ nm)}$ nanocomposites are suitable as active anode materials for LIBs.

Up to now, many electrode materials have been developed based on carbon materials and $Co_3O_4$, and all of them have some advantages and limitations. A comparison of the performance of our newly designed N-doped PC-$Co_3O_4$ with those already reported in literature is shown in Table 1. By way of comparison, it can be clearly seen that the as-prepared nanocomposites result in a relatively high reversible capacity (1060 mA h $g^{-1}$ after 100 cycles) based on the large current density at 100 mA $g^{-1}$. Remarkably, the super cyclic performance (97.7% retention during 100 cycles) and the highest initial Coulombic efficiency (86.7%) make it a promising advanced electrode material for LIBs. The excellent performance of the N-doped PC-$Co_3O_{4\ (10\ nm)}$ electrode materials may be due to the synergistic effect of the two components. First, the good conductivity and porous structure of the N-doped PC provide a highway for electron transfer and easy access for $Li^+$ to the electrode materials, which is beneficial to rate capability and Coulombic efficiencies. Second, the high specific surface area and abundant nitrogen functional groups of the N-doped PC provide more binding sites for facile deposition of $Co_3O_4$ and promote the contact of the electrolyte to the $Co_3O_4$. Third, the strong bonding between the $Co_3O_4$ nanoparticles and the N-doped PC result in the low contact resistance and the good cycling stability of the composite electrode materials. Furthermore, the simply and economically preparation process of N-doped PC-$Co_3O_4$ make it a promising electrode material for large scale production.

## 4. CONCLUSIONS

In summary, a new N-doped PC with a great potential application in practical energy storage and conversion devices was cheaply synthesized by using crawfish shell as carbon source. A facile strategy to prepare the nanocomposite of N-doped PC anchored with $Co_3O_4$ nanoparticles as a novel anode material for high performance of LIBs is proposed. The good conductivity and porous structure of the N-doped PC not only provide binding sites for facile deposition of a large number of $Co_3O_4$ nanoparticles but also provide the channels for charge and ionic transport, which effectively alleviates the aggregation of $Co_3O_4$ in the $Li^+$ insertion/extraction. As a consequence, the as-prepared N-doped PC-$Co_3O_{4\ (10\ nm)}$ nanocomposites exhibits a high reversible capacity (1060 mA h $g^{-1}$ at 100th cycle), excellent cyclic performance, good rate capability, and large initial Coulombic efficiency (86.7%). The strategy may be also extended to the synthesis of other metal oxide nanocomposites on the N-doped PC. The biomass concept will open a new avenue for producing nanostructured electrode materials from low-cost sustainable sources.

## ■ ASSOCIATED CONTENT

### Supporting Information

SEM images of N-doped PC-$Co_3O_4$ nanocomposites under different time, SEM images of N-doped PC-$Co_3O_4$ nanocomposites during different temperatures, SEM images of N-doped PC-$Co_3O_{4\ (100\ nm)}$ nanocomposites and synthesis procedure, XRD pattern, nitrogen adsorption/desorption isotherms and TGA curves of the N-doped PC-$Co_3O_{4\ (100\ nm)}$ nanocomposites, overview SEM images of a piece of N-doped PC derived from crawfish shell, XPS full-spectrum of the N-doped PC derived from crawfish shell, XPS full-spectrum and $C_{1s}$ XPS spectra of the N-doped PC-$Co_3O_{4\ (10\ nm)}$ nanocomposites, rate performance of the N-doped PC-$Co_3O_{4\ (10\ nm)}$ nanocomposites, elemental analysis of N-doped PC, calculated $R_s$, $R_f$, and $R_{ct}$ through fitting of the impedance spectra. This material is available free of charge via the Internet at http://pubs.acs.org.

## ■ AUTHOR INFORMATION

### Corresponding Author

*E-mail: yhsong@jxnu.edu.cn. Tel/Fax: +86-791-88120862.

### Notes

The authors declare no competing financial interest.

## ■ ACKNOWLEDGMENTS

This work was financially supported by National Natural Science Foundation of China (21065005, 21165010, and 21101146), Young Scientist Foundation of Jiangxi Province (20112BCB23006 and 20122BCB23011), Science and Technology Support Program of Jiangxi Province (20123BBE50104 and 20133BBE50008), Foundation of Jiangxi Educational Committee (GJJ13243 and GJJ13244), the State Key

Laboratory of Electroanalytical Chemistry (SKLEAC201310), the Open Project Program of Key Laboratory of Functional Small organic molecule, Ministry of Education, Jiangxi Normal University (KLFS-KF-201214; KLFS-KF-201218).

## REFERENCES

(1) Etacheri, V.; Marom, R.; Elazari, R.; Salitra, G.; Aurbach, D. Challenges in the Development of Advanced Li-ion Batteries: a Review. *Energy Environ. Sci.* **2011**, *4*, 3243−3262.
(2) Xin, S.; Guo, Y. G.; Wan, L. J. Nanocarbon Networks for Advanced Rechargeable Lithium Batteries. *Acc. Chem. Res.* **2012**, *45*, 1759−1769.
(3) Armand, M.; Tarascon, J. M. Building Better Batteries. *Nature* **2008**, *451*, 652−657.
(4) Wu, Z. S.; Ren, W.; Wen, L.; Gao, L.; Zhao, J.; Chen, Z.; Zhou, G.; Li, F.; Cheng, H. M. Graphene Anchored with $Co_3O_4$ Nanoparticles as Anode of Lithium Ion Batteries with Enhanced Reversible Capacity and Cyclic Performance. *ACS Nano* **2010**, *4*, 3187−3194.
(5) Liu, J.; Xia, H.; Lu, L.; Xue, D. Anisotropic $Co_3O_4$ Porous Nanocapsules Toward High-capacity Li-ion Batteries. *J. Mater. Chem.* **2010**, *20*, 1506−1510.
(6) Liu, J.; Wan, Y.; Liu, C.; Liu, W.; Ji, S.; Zhou, Y.; Wang, J. Solvothermal Synthesis of Uniform $Co_3O_4$/C Hollow Quasi-Nanospheres for Enhanced Lithium Ion Intercalation Applications. *Eur. J. Inorg. Chem.* **2012**, *2012*, 3825−3829.
(7) Zhu, X.; Ning, G.; Ma, X.; Fan, Z.; Xu, C.; Gao, J.; Xu, C.; Wei, F. High Density $Co_3O_4$ Nanoparticles Confined in a Porous Graphene Nanomesh Network Driven by an Electrochemical Process: Ultra-high Capacity and Rate Performance for Lithium Ion Batteries. *J. Mater. Chem. A* **2013**, *1*, 14023−14030.
(8) Zhu, J.; Sharma, Y. K.; Zeng, Z.; Zhang, X.; Srinivasan, M.; Mhaisalkar, S.; Zhang, H.; Hng, H. H.; Yan, Q. Cobalt Oxide Nanowall Arrays on Reduced Graphene Oxide Sheets with Controlled Phase, Grain Size, and Porosity for Li-Ion Battery Electrodes. *J. Phys. Chem. C* **2011**, *115*, 8400−8406.
(9) Qi, Y.; Zhang, H.; Du, N.; Yang, D. Highly Loaded CoO/graphene Nanocomposites as Lithium-Ion Anodes with Superior Reversible Capacity. *J. Mater. Chem. A* **2013**, *1*, 2337−2342.
(10) Liu, J.; Zhou, Y.; Liu, C.; Wang, J.; Pan, Y.; Xue, D. Self-assembled Porous Hierarchical-like CoO@C Microsheets Transformed from Inorganic-organic Precursors and Their Lithium-Ion Battery Application. *CrystEngComm* **2012**, *14*, 2669−2674.
(11) Chen, D.; Ji, G.; Ma, Y.; Lee, J. Y.; Lu, J. Graphene-Encapsulated Hollow $Fe_3O_4$ Nanoparticle Aggregates as a High-Performance Anode Material for Lithium Ion Batteries. *ACS Appl. Mater. Interfaces* **2011**, *3*, 3078−3083.
(12) Jang, B.; Park, M.; Chae, O. B.; Park, S.; Kim, Y.; Oh, S. M.; Piao, Y.; Hyeon, T. Direct Synthesis of Self-Assembled Ferrite/Carbon Hybrid Nanosheets for High Performance Lithium-Ion Battery Anodes. *J. Am. Chem. Soc.* **2012**, *134*, 15010−15015.
(13) Reddy, A. L. M.; Shaijumon, M. M.; Gowda, S. R.; Ajayan, P. M. Coaxial $MnO_2$/Carbon Nanotube Array Electrodes for High-Performance Lithium Batteries. *Nano Lett.* **2009**, *9*, 1002−1006.
(14) Qiu, M.; Yang, L.; Qi, X.; Li, J.; Zhong, J. Fabrication of Ordered NiO Coated Si Nanowire Array Films as Electrodes for a High Performance Lithium Ion Battery. *ACS Appl. Mater. Interfaces* **2010**, *2*, 3614−3618.
(15) Choi, C. S.; Park, Y. U.; Kim, H.; Kim, N. R.; Kang, K.; Lee, H. M. Three-Dimensional Sponge-Like Architectured Cupric Oxides as High-Power and Long-Life Anode Material for Lithium Rechargeable Batteries. *Electrochim. Acta* **2012**, *70*, 98−104.
(16) Yang, S.; Cui, G.; Pang, S.; Cao, Q.; Kolb, U.; Feng, X.; Maier, J.; Müllen, K. Fabrication of Cobalt and Cobalt Oxide/Graphene Composites: Towards High-Performance Anode Materials for Lithium Ion Batteries. *ChemSusChem* **2010**, *3*, 236−239.
(17) Qi, Y.; Zhang, H.; Du, N.; Zhai, C.; Yang, D. Synthesis of $Co_3O_4$@$SnO_2$@C Core-Shell Nanorods with Superior reversible Lithium-Ion Storage. *RSC Adv.* **2012**, *2*, 9511−9516.
(18) Chen, Y.; Lu, Z.; Zhou, L.; Mai, Y. W.; Huang, H. In Situ Formation of Hollow Graphitic Carbon Nanospheres in Electrospun Amorphous Carbon Nanofibers for High-Performance Li-Based Batteries. *Nanoscale* **2012**, *4*, 6800−6805.
(19) Zhai, Y.; Dou, Y.; Zhao, D.; Fulvio, P. F.; Mayes, R. T.; Dai, S. Carbon Materials for Chemical Capacitive Energy Storage. *Adv. Mater.* **2011**, *23*, 4828−4850.
(20) Wang, G.; Zhang, L.; Zhang, J. A Review of Electrode Materials for Electrochemical Supercapacitors. *Chem. Soc. Rev.* **2012**, *41*, 797−828.
(21) Chen, Y.; Lu, Z.; Zhou, L.; Mai, Y. W.; Huang, H. Triple-Coaxial Electrospun Amorphous Carbon Nanotubes with Hollow Graphitic Carbon Nanospheres for High-Performance Li Ion Batteries. *Energy Environ. Sci.* **2012**, *5*, 7898−7902.
(22) Zheng, W.; Lu, X.; Wong, S. C. Electrical and Mechanical Properties of Expanded Graphite-Reinforced High-Density Polyethylene. *J. Appl. Polym. Sci.* **2004**, *91*, 2781−2788.
(23) Jiang, H.; Lee, P. S.; Li, C. Z. 3D Carbon Based Nanostructures for Advanced Supercapacitors. *Energy Environ. Sci.* **2013**, *6*, 41−53.
(24) Vu, A.; Qian, Y.; Stein, A. Porous Electrode Materials for Lithium-Ion Batteries-How to Prepare Them and What Makes Them Special. *Adv. Energy Mater.* **2012**, *2*, 1056−1085.
(25) Lee, J.; Kim, J.; Hyeon, T. Recent Progress in the Synthesis of Porous Carbon Materials. *Adv. Mater.* **2006**, *18*, 2073−2094.
(26) Wang, H.; Gao, Q.; Hu, J. High Hydrogen Storage Capacity of Porous Carbons Prepared by Using Activated Carbon. *J. Am. Chem. Soc.* **2009**, *131*, 7016−7022.
(27) Pumera, M. Graphene-Based Nanomaterials for Energy Storage. *Energy Environ. Sci.* **2011**, *4*, 668−674.
(28) White, R. J.; Antonietti, M.; Titirici, M.-M. Naturally Inspired Nitrogen Doped Porous Carbon. *J. Mater. Chem.* **2009**, *19*, 8645−8650.
(29) Brun, N.; Prabaharan, S. R.; Surcin, C.; Morcrette, M.; Deleuze, H.; Birot, M.; Babot, O.; Achard, M. F.; Backov, R. Design of Hierarchical Porous Carbonaceous Foams from a Dual-Template Approach and Their Use as Electrochemical Capacitor and Li Ion Battery Negative Electrodes. *J. Phys. Chem. C* **2011**, *116*, 1408−1421.
(30) Liang, C.; Li, Z.; Dai, S. Mesoporous Carbon Materials: Synthesis and Modification. *Angew. Chem., Int. Ed.* **2008**, *47*, 3696−3717.
(31) Polarz, S.; Smarsly, B.; Schattka, J. H. Hierachical Porous Carbon Structures from Cellulose Acetate Fibers. *Chem. Mater.* **2002**, *14*, 2940−2945.
(32) Xia, Y.; Zhang, W.; Xiao, Z.; Huang, H.; Zeng, H.; Chen, X.; Chen, F.; Gan, Y.; Tao, X. Biotemplated Fabrication of Hierarchically Porous NiO/C Composite from Lotus Pollen Grains for Lithium-Ion Batteries. *J. Mater. Chem.* **2012**, *22*, 9209−9215.
(33) Zhang, J.; Xiang, J.; Dong, Z.; Liu, Y.; Wu, Y.; Xu, C.; Du, G. Biomass Derived Activated Carbon with 3D Connected Architecture for Rechargeable Lithium-sulfur Batteries. *Electrochim. Acta* **2014**, *116*, 146−151.
(34) Yao, H.; Zheng, G.; Li, W.; McDowell, M. T.; Seh, Z.; Liu, N.; Lu, Z.; Cui, Y. Crab Shells as Sustainable Templates from Nature for Nanostructured Battery Electrodes. *Nano Lett.* **2013**, *13*, 3385−3390.
(35) Kurosaki, F.; Koyanaka, H.; Tsujimoto, M.; Imamura, Y. Shape-Controlled Multi-Porous Carbon with Hierarchical Micro-Meso-Macro Pores Synthesized by Fash Heating of Wood Biomass. *Carbon* **2008**, *46*, 850−857.
(36) Li, J.; Xu, Q.; Wang, J.; Jiao, J.; Zhang, Z. Controlled Synthesis of Monolithic Hierarchical Porous Materials Using Wood as a Template with Assistance of Supercritical Carbon Dioxide. *Ind. Eng. Chem. Res.* **2008**, *47*, 7680−7685.
(37) Hu, Y. S.; Adelhelm, P.; Smarsly, B. M.; Hore, S.; Antonietti, M.; Maier, J. Synthesis of Hierarchically Porous Carbon Monoliths with Highly Ordered Microstructure and Their Application in Rechargeable

Lithium Batteries with High-Rate Capability. *Adv. Funct. Mater.* **2007**, *17*, 1873−1878.
(38) Cho, Y. J.; Kim, H. S.; Im, H.; Myung, Y.; Jung, G. B.; Lee, C. W.; Park, J.; Park, M.-H.; Cho, J.; Kang, H. S. Nitrogen-Doped Graphitic Layers Deposited on Silicon Nanowires for Efficient Lithium-Ion Battery Anodes. *J. Phys. Chem. C* **2011**, *115*, 9451−9457.
(39) Stein, A.; Wang, Z.; Fierke, M. A. Functionalization of Porous Carbon Materials with Designed Pore Architecture. *Adv. Mater.* **2009**, *21*, 265−293.
(40) Qie, L.; Chen, W. M.; Wang, Z. H.; Shao, Q. G.; Li, X.; Yuan, L. X.; Hu, X. L.; Zhang, W. X.; Huang, Y. H. Nitrogen-Doped Porous Carbon Nanofiber Webs as Anodes for Lithium Ion Batteries with a Superhigh Capacity and Rate Capability. *Adv. Mater.* **2012**, *24*, 2047−2050.
(41) Wu, Z. S.; Ren, W.; Xu, L.; Li, F.; Cheng, H. M. Doped Graphene Sheets as Anode Materials with Superhigh Rate and Large Capacity for Lithium Ion Batteries. *ACS Nano* **2011**, *5*, 5463−5471.
(42) Bulusheva, L.; Okotrub, A.; Kurenya, A.; Zhang, H.; Zhang, H.; Chen, X.; Song, H. Electrochemical Properties of Nitrogen-Doped Carbon Nanotube Anode in Li-Ion Batteries. *Carbon* **2011**, *49*, 4013−4023.
(43) Poizot, P.; Laruelle, S.; Grugeon, S.; Dupont, L.; Tarascon, J. Nano-Sized Transition-Metal Oxides as Negative-Electrode Materials for Lithium-Ion Batteries. *Nature* **2000**, *407*, 496−499.
(44) Mei, W.; Huang, J.; Zhu, L.; Ye, Z.; Mai, Y.; Tu, J. Synthesis of Porous Rhombus-Shaped $Co_3O_4$ Nanorod Arrays Grown Directly on a Nickel Substrate with High Electrochemical Performance. *J. Mater. Chem.* **2012**, *22*, 9315−9321.
(45) Yang, X.; Fan, K.; Zhu, Y.; Shen, J.; Jiang, X.; Zhao, P.; Li, C. Tailored Graphene-Encapsulated Mesoporous $Co_3O_4$ Composite Microspheres for High-Performance Lithium Ion Batteries. *J. Mater. Chem.* **2012**, *22*, 17278−17283.
(46) Liang, Y.; Wang, H.; Diao, P.; Chang, W.; Hong, G.; Li, Y.; Gong, M.; Xie, L.; Zhou, J.; Wang, J. Oxygen Reduction Electrocatalyst Based on Strongly Coupled Cobalt Oxide Nanocrystals and Carbon Nanotubes. *J. Am. Chem. Soc.* **2012**, *134*, 15849−15857.
(47) Li, Z.; Lu, C.; Xia, Z.; Zhou, Y.; Luo, Z. X-ray Diffraction Patterns of Graphite and Turbostratic Carbon. *Carbon* **2007**, *45*, 1686−1695.
(48) Meng, X.; Zhong, Y.; Sun, Y.; Banis, M. N.; Li, R.; Sun, X. Nitrogen-Doped Carbon Nanotubes Coated by Atomic Layer Deposited $SnO_2$ with Controlled Morphology and Phase. *Carbon* **2011**, *49*, 1133−1144.
(49) Wang, H.; Zhang, C.; Liu, Z.; Wang, L.; Han, P.; Xu, H.; Zhang, K.; Dong, S.; Yao, J.; Cui, G. Nitrogen-Doped Graphene Nanosheets with Excellent Lithium Storage Properties. *J. Mater. Chem.* **2011**, *21*, 5430−5434.
(50) Chen, J.; Xia, X. H.; Tu, J. P.; Xiong, Q. Q.; Yu, Y. X.; Wang, X. L.; Gu, C. D. $Co_3O_4$-C Core-Shell Nanowire Array as an Advanced Anode Material for Lithium Ion Batteries. *J. Mater. Chem.* **2012**, *22*, 15056−15061.
(51) Zhuo, L.; Wu, Y.; Ming, J.; Wang, L.; Yu, Y.; Zhang, X.; Zhao, F. Facile Synthesis of a $Co_3O_4$-Carbon Nanotube Composite and its Superior Performance as an Anode Material for Li-Ion Batteries. *J. Mater. Chem. A* **2013**, *1*, 1141−1147.
(52) Li, D.; Shi, D.; Chen, Z.; Liu, H.; Jia, D.; Guo, Z. Enhanced Rate Performance of Cobalt Oxide/Nitrogen Doped Graphene Composite for Lithium Ion Batteries. *RSC Adv.* **2013**, *3*, 5003−5008.
(53) Li, W. Y.; Xu, L. N.; Chen, J. $Co_3O_4$ Nanomaterials in Lithium-Ion Batteries and Gas Sensors. *Adv. Funct. Mater.* **2005**, *15*, 851−857.
(54) Wu, H.; Xu, M.; Wang, Y.; Zheng, G. Branched $Co_3O_4/Fe_2O_3$ Nanowires as High Capacity Lithium-Ion Battery Anodes. *Nano Res.* **2013**, 1−7.
(55) Kim, G. P.; Nam, I.; Kim, N. D.; Park, J.; Park, S.; Yi, J. A Synthesis of Graphene/$Co_3O_4$ Thin Films for Lithium Ion Battery Anodes by Coelectrodeposition. *Electrochem. Commun.* **2012**, *22*, 93−96.
(56) Yue, J.; Zhao, X.; Xia, D. Electrochemical Lithium Storage of C/Co Composite as an Anode Material for Lithium Ion Batteries. *Electrochem. Commun.* **2012**, *18*, 44−47.
(57) Zhang, P.; Guo, Z. P.; Huang, Y.; Jia, D.; Liu, H. K. Synthesis of $Co_3O_4$/Carbon Composite Nanowires and Their Electrochemical Properties. *J. Power. Sources* **2011**, *196*, 6987−6991.
(58) Hao, F.; Zhang, Z.; Yin, L. $Co_3O_4$/Carbon Aerogel Hybrids as Anode Materials for Lithium-Ion Batteries with Enhanced Electrochemical Properties. *ACS Appl. Mater. Interfaces* **2013**, *5*, 8337−8344.
(59) Choi, B. G.; Chang, S. J.; Lee, Y. B.; Bae, J. S.; Kim, H. J.; Huh, Y. S. 3D Heterostructured Architectures of $Co_3O_4$ Nanoparticles Deposited on Porous Graphene Surfaces for High Performance of Lithium Ion Batteries. *Nanoscale* **2012**, *4*, 5924−5930.
(60) Chen, S. Q.; Wang, Y. Microwave-Assisted Synthesis of a $Co_3O_4$-Graphene Sheet-on-Sheet Nanocomposite as a Superior Anode Material for Li-ion Batteries. *J. Mater. Chem.* **2010**, *20*, 9735−9739.
(61) Yang, X.; Fan, K.; Zhu, Y.; Shen, J.; Jiang, X.; Zhao, P.; Luan, S.; Li, C. Electric Papers of Graphene-Coated $Co_3O_4$ Fibers for High-Performance Lithium-Ion Batteries. *ACS Appl. Mater. Interfaces* **2013**, *5*, 997−1002.